Experimental and Numerical Analysis of Opaque Turbulent Buoyant Jet

A. B. Osman [1†], M. Ovinis[1], M. H. Fakhruldin [1] and I. Faye [2]

[1] *Mechanical Engineering Department, Universiti Teknologi PETRONAS 32610 Seri Iskandar, Perak, Malaysia*
[2] *Fundamental & Applied Science Department, Universiti Teknologi PETRONAS 32610 Seri Iskandar, Perak, Malaysia*

†*Corresponding* Author's Emails: osmanano68@gmail.com

ABSTRACT

Opaque fluid flow estimation is a challenging problem due to the complex nature of this flow type. Deepwater Horizon oil spill is one of the real examples of opaque fluid flow. Due to the complicated spill flow and the lack of dedicated flow measurement technique its flow rate was estimated with high uncertainty. In this paper, a simulation of jet flow is conducted experimentally and numerically. This is in order to analyze the difference between them. First, a turbulent buoyant jet was experimentally simulated considering various ranges of nozzle flow rates including laminar and turbulent flow. A video camera was used to capture the jet flow. Then, Fast Fourier Transform (FFT) based method was developed to estimate velocity field from video sequence. The outcomes of experimental results were compared to the outcomes of numerical simulation. As a result, the FFT-based method was estimated the nozzle flow rates with a relative error of 18.2% when it was compared to the measured experimental values. Despite this poor accuracy, a good agreement between experimental and numerical simulation outcomes was found in term of overall velocity field, centerline velocity, axial velocity as well as the distribution of radial velocity.

1. INTRODUCTION

A turbulent buoyant jet is referred to a flow-type in which two fluids have different densities mixed together. An example of turbulent buoyant jet flow is a deepwater oil spill in which the spilled oil mixes with seawater which has a different density. Black smoker or hydrothermal vent is also another example of a turbulent buoyant jet, in which hydrocarbon leaks into seawater. The study of such flow type is an important task to understand its flow dynamics. This can help to know the velocity field, initial flow rate, as well as quantifying the amount of spilled oil/hydrocarbon into the environment. Then, an appropriate response such as the cleanup process can be taken in order to minimize their negative effects on the environment. The importance of jet flow study arises in numerous fields either industrial applications or natural flows such as waste disposal systems, and smoke plumes from chimneys. Turbulent buoyant jet such as deepwater oil spill can be described as an opaque fluid. The theory of jet flow suggested that the velocity field at a jet center plane is closer to the actual velocity. However, for an opaque fluid, only the jet surface can be seen, and its center plane is invisible when using an optical sensor to capture the fluid flow, leading to increasing the challenges of velocity field estimation. This is due to the complex nature of the velocity field at the jet surface.

Several researchers studied the behaviour of turbulent buoyant jet experimentally (Tian and P. J. Roberts. 2003; Mi, Nobes, & Nathan. 2001). Turbulent buoyant jet flow behavior is usually affected by its initial conditions at the jet exist, includes nozzle Reynold's number, nozzle geometry and density ratio between the two fluids. The significance of initial conditions on the development of a turbulent jet flow was investigated by (Abdel-Rahman 2010; Bradshaw. 1966; Dziomba & Fiedler. 1985). However, the effect of initial conditions on jet velocity field distribution beyond the jet exit is less conclusive. They concluded that in case of Reynolds number of the jet exit is greater than a few thousand, the radial

spread of mean velocity field and decay of centerline velocity in downstream direction are independent of Reynold's number. Abdel-Rahman (Abdel-Rahman, 2010) stated that by increasing Reynold's number at jet exist more than 20,000, the jet entrainment will increase and will become constant more than that. By increasing Reynold's number, various flow behaviors can be observed includes a laminar flow at low Reynold's too turbulent flow behavior at high Reynold's value. The effect of nozzle geometry, including orifice plate, profiled nozzle, or a pipe, and their influence on jet flow behavior was investigated by (Mi and Nathan. 2010; Mi, Kalt, Nathan & Wong. 2007; Mi, Nathan & Luxton. 2000; Quinn. 2006 & 2007). Different flow behaviors can be obtained by changing the nozzle geometry, in which around jet produces axisymmetric jet flow behavior. In their works, several parameters were experimentally investigated, including mean axial and radial velocity distribution, decay of centerline velocity, and jet spread rate. By increasing the Reynolds numbers at jet exist; both decays of centerline velocity and radial velocity were increased. One of the important properties of the turbulent jet is a self-similarity property of fully-developed region. The normalization of radial velocity at different axial distances provides a similarity property which should have Gaussian profiles. Extensive works were done before to investigate the self-similarity of jet flow at the fully developed region (Abdel-Rahman. 2010; Wygnanski & Fiedler. 1969; Uddin & Pollard. 2007).

A turbulent buoyant jet was investigated using a numerical simulation. One of the common techniques for fluid flow simulation is the computational fluid dynamics (CFD). CFD uses numerical approaches to solve fluid flow problems. Several models have been proposed to simulate fluid dynamics when using CFD such as direct numerical simulation (DNS), Large Eddy Simulation (LES), Reynolds Average Navier-Stokes (RANS), Detached Eddy Simulation (DES). A proper selection of these models is mainly based on model accuracy as well as its computational time. The turbulent buoyant jet flow was simulated numerically by (Wang *et al.* 2010; Muppidi & Mahesh. 2005), where the DNS model was applied. DNS model is based on solving Navier-Stokes equations and has good accuracy as compared to other models. However, the main drawback of DNS is the high computational time associated with the model. LES model is a good option for numerical simulation of turbulent flow with less computational time. This is because the LES model ignores the smallest scales of turbulent flow. LES is an appropriate model for dealing with fluid flow, which has large-scale motion. Several researchers applied LES for fluid flow simulation and investigated a turbulent jet flow characteristics. Akselvoll *et al.* (1996) investigated on the flow behavior of a confined turbulent jet, while (Kannan, Karthikeyan, & Sundararaj. 2017) were studied an axisymmetric jet flow. However, the LES model was limited to resolve fluid flow in near-wall regions, where the turbulent length is less than the

maximum size of the simulation grid. To overcome this problem LES was usually combined with the RANS model. RANS model has the advantage of considering the small scales of turbulent flow, while LES presents the larger scales. This hybrid model (i.e. LES-RANS) is also called the DES model (Spalart, Jou, Strelets, & Allmaras. 1997). RANS solve the fluid problem based on solving Reynolds equations. These equations are the averaged forms of Navier-Stokes equations. For this reason, the RANS can be described as a time-averaged model. K-epsilon models have extensive applications in fluid dynamics. The K-epsilon model considers two variables, namely, turbulent kinetic energy, and the dissipation rate of kinetic energy. K-epsilon model has three forms, including standard k-epsilon, realizable k-epsilon, and RNG k-epsilon model. The standard k-epsilon model has a degree of advantage of fast convergence rate, relatively low memory requirements, as well as it has higher accuracy (Sorbe. 2014). The standard k-epsilon model estimates turbulent viscosity based on a linear turbulence scale. The RNG model developed by (Yakhot *et al.* 1992) was based on solving mathematical methods of Reynolds Normalization Group (RNG). It has the advantage of considering different turbulent flow scales. Shih *et al.* (1995) proposed a realizable k-epsilon model as an improvement of the standard k-epsilon model. The realizable k-epsilon model is based on new formulations of turbulent viscosity and transport equations of dissipation rate, which differ from the standard model. The term "realizable" means that the model satisfies certain mathematical constraints on the Reynolds stresses, consistent with the physics of turbulent flows. Kannan *et al.* (2017), simulated an axisymmetric turbulent jet flow using various turbulence models in order to compare their accuracy in the prediction of turbulent jet flow. Two groups of models were used, including first-order models (i.e. standard k-epsilon model, standard k-omega model, RNG k-epsilon, realizable k-epsilon model, SST k-omega model), and a second-order model (i.e. Reynolds stress model). In their work, several parameters were investigated, including decay of centerline velocity, turbulence intensity, kinetic energy, and streamlines. The outcomes of this simulation were compared to the available experimental data. In all cases, the first-order models accurately predicted the jet flow as compared to the results of the second-order model with large variations. Aziz *et al.* (2008) were simulated a turbulent jet flow in order to predict jet centerline velocity, radial velocity, growth rate, and turbulent kinematic energy. They investigated both round and plane turbulent jet flow, in which the three forms of k-epsilon models were applied. The outcomes of the simulation were compared with the prediction of the theory of jet flow. They concluded that the k-epsilon model with standard coefficients outperformed the others for both round and plane turbulent jets flow characteristics.

On the other hand, several techniques were developed for fluid flow measurement, which can be categorized into invasive and non-invasive techniques. Invasive techniques are that technique

in a direct contact with the fluid, while the non-invasive techniques are those measures the flow without direct contact with the fluid. Invasive techniques are more appropriate for fluid flow measurement in pipelines and when the local measurement is required (Miller. 1983). An example of an invasive technique is a pressure probe (Chue. 19750; Bailey *et al*. 2013), and Hot Wire Anemometry (Stainback & Nagabushana. 1993). However, these techniques suffer from several drawbacks that result in an inaccurate estimation of the flow. First, it is a point-by-point measurement technique, in which only the velocity of one or a few points can be measured. Second, it is sensitive to various environmental parameters such as temperature, humidity as well as the need for prior calibration. Inaccuracies can result due to the direct contact of those devices with the fluid which leads to obstructions as well as the probability of the instrument to break during measurement. Furthermore, the invasive techniques are not applicable for real turbulent buoyant jet flow estimation such Deepwater oil spill. This is due to the limited temporal and spatial resolution of these techniques. Optical techniques are examples of a non-invasive technique that has been used for flow measurement. They have been appropriate for environmental flow measurement (McNutt *et al.* 2012; McNutt *et al.* 2011), as well as it can be used for laboratory scale (Crone, McDuff & Wilcock. 2008). The non-invasive techniques have better temporal and spatial resolution, from which a full velocity field can be obtained. Next, it had solved the problem of measurement uncertainty that comes as a result of flow disturbance associated with the invasive techniques. This is because the optical sensor is not in a direct contact with the fluid during the measurement process. However, the accuracy of the optical technique is based on the quality of input images as well as the accuracy of the algorithm could be used for image velocity field estimation.

In the same context, optical techniques can be classified based on their imaging technique into active and passive technique. Active techniques usually use an internal illumination for flow area visualization such as laser sheet or spot, while passive technique usually uses an external illumination source for flow visualization. An example of the active technique is Particle Image Velocimetry (PIV) which is a powerful technique for flow visualization and flow estimation and has wide ranges of applications in fluid dynamics (Adrian. 1991). The use of laser sheet provides detailed information about the fluid flow, including both fine and large scales of motion. This will help in a better flow visualization and measurement. However, the active technique requires complicated imaging system components, which limits its use for deepwater oil spill visualization. PIV was accurately measured fluid flow at the laboratory scale only. This because of the use of pulsed light sources (e.g. Nd: YAG laser4 with short pulses of ~5 ns), lead to reducing motion blur of fluid particles. However, the active imaging system requires a stable and calibrated position during data collection, which limits its use for underwater

applications. To overcome this problem, a passive imaging system can be easily used in the deepwater environment. This is because it uses simple components such as video cameras with halogen or LED lights. An example of a passive optical technique is optical plume velocimetry (OPV). The use of passive imaging system has been appropriate for data acquisition of oil spill (McNutt *et al*. 2012). However, the use of passive techniques increases the challenge of collecting high-quality data. This difficulty in flow visualization is associated with the use of a permanent light source, leading to smearing of high-contrast flow structures. However, by developing a good algorithm for image velocity field estimation, the passive optical technique can be applicable for real flow estimation with high accuracy. However, an oil jet is an opaque flow and its estimation is challenging. This is due to the difficulty of optically accessing the oil jet center plane and acquire velocity field closer to the actual field. Therefore, the only option for the estimation of opaque jet flow is the estimation of the surface structure.

In this work, a turbulent buoyant jet was experimentally and numerically simulated. A passive imaging system was used to the jet flow video at several ranges of nozzle flow rates. The velocity field was estimated from a video image sequence using Fast Fourier Transform (FFT) based method. Next, CFD was utilized for the simulation of jet flow considering the same ranges of flow rates of experimental work.

2. METHOD

This section describes the overall methodology of this work, including a detailed description of an experimental facility used and flow rate measurement method, and the steps for numerical simulation of the turbulent buoyant jet.

2.1 Experimental Facility

Figure 1 shows the layout of the experimental setup used for simulating a turbulent buoyant jet. For each experimental run, the jet flow was simulated by allowing a fluid from the overhead tank to flow to the main tank through a nozzle with a diameter of 10 mm. The nozzle flow rate was controlled by a control valve fixed between the overhead tank and the nozzle. The fluid in the overhead tank is made up of tap water, salt (i.e. NaCl of 5 % weight), and colloidal graphite while the main tank was filled with tap water. Graphite was used to provide better visualization of the flow and for improving the quality of the video while the salt was used to provide the buoyancy effect in the turbulent jet flow, as recommended by (Crone, McDuff & Wilcock. 2008). The mixed fluid was first prepared in the supply tank and pumped to the overhead tank using a submersible pump. During the experimental runs, the level of fluid in the overhead tank should be maintained to provide constant flow rate at the nozzle so that excess fluid will flow through the return line back to the supply tank. The main tank was made of a transparent acrylic material with a
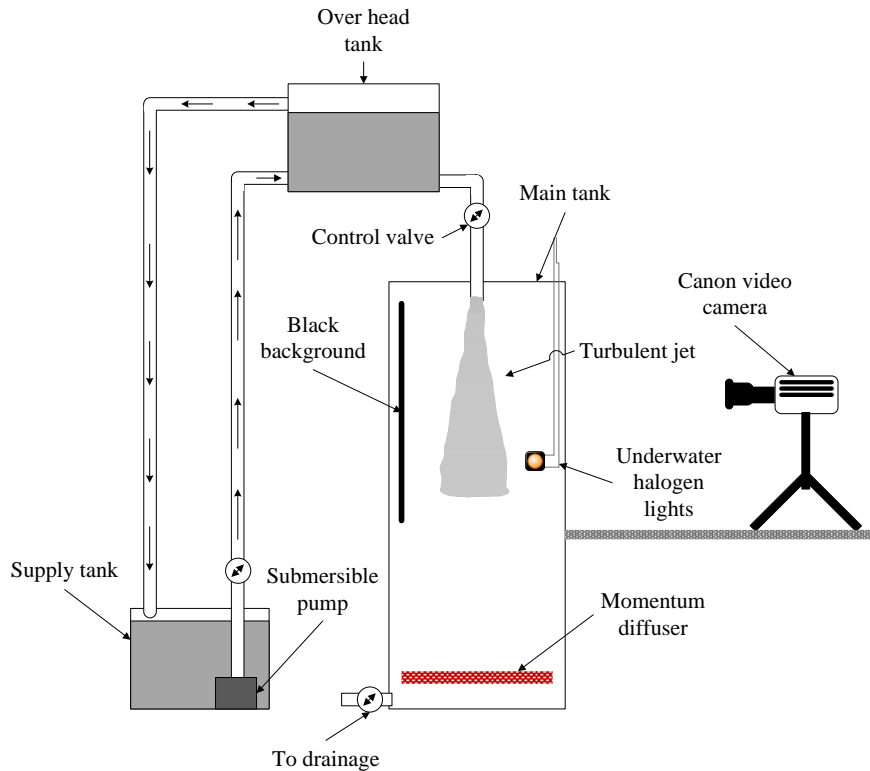
Fig. 1. Experimental set-up used for turbulent buoyant jet simulation.

dimension of 900 x 900 x 2000 mm, which was big enough to accommodate the fluid mixture. A momentum diffuser was put inside the main tank to keep the black fluid in the bottom of the tank while a valve fixed at the bottom of the main tank is for drainage purpose.

2.1.2 Flow Rate Measurement

Knowing the actual flow rates of a turbulent buoyant jet flow is important to validate the proposed FFT based algorithm. The actual flow rates of the turbulent buoyant jet were measured at the jet exist by calibrating the opening of the control valve (Crone, McDuff & Wilcock. 2008). For each run of the experiment, the submersible pump was used in order to pump the mixture of fluid to overhead tank. By opening the control valve, the mixture fluid will go into the main tank and simulate the turbulent buoyant jet. The control valve opening was calibrated by measuring the time that allows 5 liters of jet fluid to pass through the control valve.

Table 1 summarizes the five cases of flow rates considered in this work. For each case, the jet flow rate Q_i was calculated by dividing the volume of jet fluid over the time required to pass the control valve. An average of flow rate Q_m with its percentage of standard deviation S normalized by the average flow rates was calculated. The nozzle velocity was calculated by dividing the averaged nozzle flow rate Q_m, over the cross-sectional area of nozzle A, and then the Reynolds number (Re) at jet exist was calculated using Eq. (1):

$$Re = \frac{\rho U d}{\mu} \tag{1}$$

where, ρ is fluid density, U nozzle velocity, d is nozzle diameter, and μ is fluid viscosity.

Two underwater lights have 5W-LED were placed in the main tank for flow illumination purpose. A black background was used to improve the visibility of the flow. A 10x10mm checkboard pattern was used for calibration purposes. Then, Canon EOS-550 video camera was used to collect the jet flow data for the five cases of nozzle flow rates. To include all jet flow regimes (i.e. pure jet, transitional, and fully developed regime), the camera distance from the nozzle, focal length, focusing level, and the camera field of view was adjusted. The camera was used to record a 60-sec video for each experimental run, using a frame rate of 50 fps with a resolution of 1280×720 pixels and a standard focal length of 50 mm.

2.1.3 Image Velocity Field Estimation

To estimate the image velocity field from a video sequence, an FFT-based method was used. The FFT-based algorithm estimates the velocity field based on two-point cross-correlation. Figure 2 shows the concept of velocity field estimation using the FFT-based algorithm, in which the idea presented on a sample of the image extracted from the collected video.

Table 1 Measured nozzle flow rates.

Run No.	Time (sec)	Q_i (liter/sec)	Q_m(liter/sec)	S (%)	U_m (m/sec)	Re
1	340	0.015	0.0145	3.98	0.18	1847
	351	0.014				
	348	0.014				
	332	0.015				
2	188	0.027	0.0255	3.92	0.32	3248
	197	0.025				
	203	0.025				
	200	0.025				
3	143	0.035	0.035	2.33	0.45	4459
	138	0.036				
	145	0.034				
	141	0.035				
4	101	0.05	0.04875	5.39	0.62	6210
	111	0.045				
	102	0.049				
	98	0.051				
5	54	0.093	0.092	4.04	1.16	11656
	56	0.089				
	57	0.088				
	52	0.096				
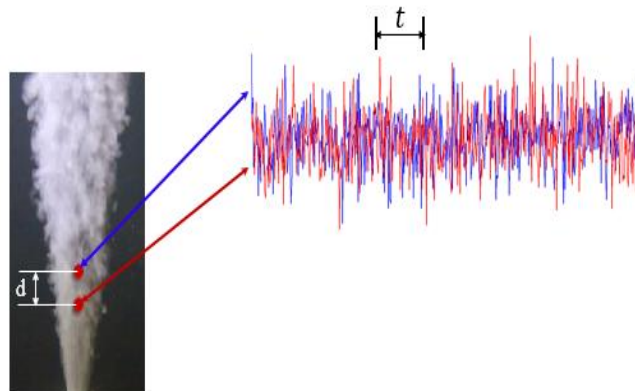
Fig. 2. Velocity field estimation using the FFT-based method.

The local velocity can be estimated by setting a separation distance d and extracting two signals (with red and blue color). Then estimate the time lag between the two signals, the velocity can be estimated by dividing the separation distance over the time lag by using Eq. (3). To estimate the velocity field using FFT, four steps are required: first, setting a separation distance between two points in the turbulent flow space and extract signals from those points. The extracted signals represent the image intensity variation at those points. Second, a cross-correlation between the two signals. Third, for accurate time lag estimation between the two signals, an interpolation of cross-correlation coefficients is required. Fourth, time lag estimation by detecting the peak of interpolated correlation coefficients.

$$U = \frac{d}{t} \qquad (2)$$

By repeating the previous four steps, the overall image velocity field can be obtained. The accuracy of velocity estimation mainly depends on both separation distance and time lag estimation algorithm. Selection of separation distance was based on the need for large time lag value between the two extracted signals. This is because a larger time lag provides higher measurement accuracy (Crone, McDuff & Wilcock. 2008). However, a larger time lag reduces the correlation between signals. The selection of too small distance will lead to a small time lag value, which may be difficult to detect. Therefore, the separation distance was fixed to be 5 pixels to estimate the image velocity field from the input image sequence for all cases of nozzle flow rates. While an accurate time-lag estimation is based on the accuracy of the cross-correlation algorithm. Fast Fourier Transform (FFT) was applied for cross-correlation step.

FFT cross correlation is based on measuring the similarity between two signals in the frequency domain. FFT cross-correlation is a classical algorithm for similarity measure between two signals/images and it has many applications such as for time lag estimation (Gilbert and Johnson. 2003). Extensive use of FFT with the common PIV

technique was introduced by (Pust. 2000). The FFT algorithm was used for correlation coefficient estimation between the extracted two signals.

If two signals are delayed by a time lag value of t, this lag can be estimated using the FFT cross-correlation algorithm in three steps: finding the Fourier transform of the two signals, multiplying them together, and finding the inverse FFT of the multiplication results to give the required correlation coefficients.

The FFT cross-correlation algorithm is represented by Eq. (3):

$$R_{FFT}(\tau) = FFT(S_2) .* \left(IFFT(S_{\partial}) \right) \qquad (3)$$

where S_1, S_2 are input signal and delayed signal respectively, * denotes the complex conjugate. The FFT of a signal of has functioned $f(n)$ with the length of n is given by:

$$F(x) = \sum_{n=0}^{N-1} f(n) e^{-j 2\pi \left(\frac{n}{N} x \right)} \qquad (4)$$

and the inverse FFT is given by:

$$f(n) = \frac{1}{N} \sum_{n=0}^{N-1} F(x) e^{-j 2\pi \left(\frac{n}{N} x \right)} \qquad (5)$$

where $F(x)$ is represent the signal $f(n)$ in frequency domain.

Once the correlation coefficient is estimated, the required time lag L_{FFT} can be obtained by detecting the maximum of these coefficients which can be formulated as:

$$L_{FFT} = \arg_t \max \left[R_{FFT}(\tau) \right] \qquad (6)$$

Post-processing of Velocity Field

Since the image velocity field is estimated, three post-processing steps were applied: first, filtering of velocity field using a median filter. This is in order to remove the velocities outliers. Second, a scaling process was applied to the filtered image velocity field. This is in order to transfer the surface velocity field to the jet center plane. This is in order to be comparable with the outcomes of numerical simulation. Third, flow regime segmentation to remove un-necessary velocity vectors found the image background.

Median Filter

A median filter is a common algorithm for improving the quality of output velocity field. This algorithm removes the velocity outliers based on replacing these outliers by their median within the defined window size. The median filter method was first proposed by (Westerweel. 1994) and applied to remove the spurious velocity vectors obtained from PIV analysis. A window size of a 5×5 pixel was used to remove the outliers of estimated velocities. The final velocity at a local point in the jet flow

region was estimated by averaging these velocities after removing its outliers. Moreover, the final velocity field was smoothed using a simple convolution of the data with a window size of 55 pixels.

Scaling of Velocity Field

Scaling of image velocity field is required since the estimated velocity vectors were representative for the jet surface velocity field. The scaling process is important in order to transfer the surface velocity field to the jet center plane. By assuming axisymmetric turbulent jet flow, the Gaussian profile can be used to relate the estimated image velocity U_{est} to the centerline velocity U_C using Equation (Lehr *et al.* 2010):

$$U_C = U_{est} e^{\left(\left(r_{/x} \right)^2 \left(x_{/\delta} \right) \ln(2) \right)} \qquad (7)$$

where U_C is the centerline velocity, r is the radial distance from the centerline, and δ is the half width of the jet, defined to be the location where the centerline velocity falls to half its value. The jet half-width increases linearly with x in the far-field, so that the jet spread rate $\delta_{/x}$ is a constant. The spread δ/x was taken to be 0.182 for round turbulent buoyant jet (Lehr *et al.* 2010). The uncertainty of centerline velocity measurement is mainly based on the uncertainty in axial distance x and radial distance r measurement. While the uncertainty of radial distance seen more significant as compared to the axial distance. This because the radial distance estimation is based on the accuracy of the method used for jet boundary detection.

2.2 Flow Regime Segmentation

Flow regime segmentation is an important step to focus the analysis only on the region where the jet flow is expected. To establish the region where the jet flow is expected, Otsu's thresholding method (Otsu. 1975) was applied. The Otsu method segments flow region by assuming that the image consists of two classes: background and foreground. By calculating the optimum threshold value between these two classes, the flow regime can be differentiated from image background.

2.3 Numerical Simulation of Turbulent Buoyant Jet

Numerical simulation has become an important tool for solving engineering problems and has extensive applications in the last few years. By using numerical simulation, complex problems can be solved. Computational Fluid Dynamics (CFD) is one of the common numerical simulation techniques used for solving fluid flow problems, including prediction of fluid flow, heat and mass transfer, chemical reactions and related phenomena. CFD solves sets of governing equations numerically in order to find a solution for flow problem. The capability of CFD as a tool is widely known in many applications. The next section describes the steps for numerical simulation of the turbulent buoyant jet in which the same range of flow rates

measured (see Table 1) from experimental work was considered.

CFD has proved its capability in simulating turbulent jet flow and can be confidently used for predicting the jet flow for different flow rate ranges. The simulation of the turbulent buoyant jet using CFD requires several steps. Figure 3 shows the procedures for CFD simulation of jet flow which includes the creation of jet geometry, mesh generation, set of boundary conditions, and define the fluid model solver, running simulation and finally results from the analysis. The next section discusses these steps in detail.
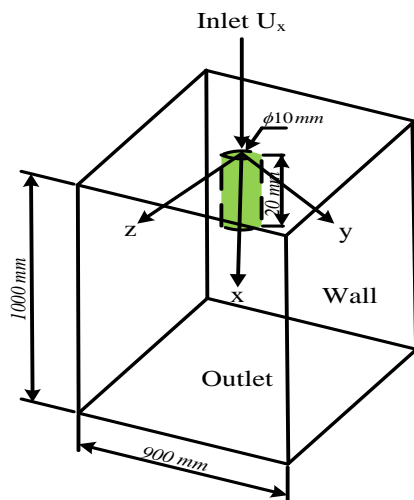
Fig. 3. Fluid domain used in CFD simulation.

2.6.1   Creation of Jet Geometry

The first step for turbulent buoyant jet simulation using CFD is the creation of jet geometry, which defines the fluid domain. Figure 3 shows the jet geometry with its coordinates considered in this study. The jet geometry dimension and the boundary conditions are selected according to the experimental work discussed in the previous section. This is for comparison and validation purpose. The jet geometry consists of a rectangular box of size 900 x 900 x 1000 mm. The jet nozzle at the upper surface has a diameter of 10 mm (as in experimental work). The nozzle (in green) is immersed in the water with a height of 20 mm, which is enough to avoid the negative effect of surface movement on the quality of video that will be recorded.

2.6.2   Mesh Generation

Mesh quality is an important factor for numerical simulation. The accuracy of the CFD simulation is mainly based on two factors: the proper setting of mesh to the geometry and the number of iterations in the solution step. There are several factors that govern the selection of meshing technique and they can be summarized in these points: the desired solution accuracy, available memory, size and shape of the geometry, quality of the starting surface mesh and the simulation topology. Different structures are available for geometry meshing

which include triangular, or quadrilateral for 2D geometry as introduced by Versteeg *et al.* (2007). In this work, a tetrahedral meshing technique is used, because it is more appropriate for meshing a 3D geometry. This mesh-type has the advantage of generating high mesh quality boundary layer by creating structured grids. This property is important to capture the fast changes in velocity at the inlet of turbulent jet flow considered in this study. The influence of mesh quality is included in the resulting chapter of this work.

2.6.3   Mesh Sensitivity Analysis

One of the important factors that affect the accuracy of the numerical simulation is the meshing structure. Figure 4 shows the mesh structure used for the jet flow simulation. In this section, mesh dependency was investigated in order to establish the proper mesh to use for the turbulent buoyant jet simulation. Finding the optimum number of mesh elements is important to help in ensuring better results and to reduce the computational time. This is because the selection of more elements usually requires a high-performance computer with higher RAM as the computational time increases with increasing the number of elements.
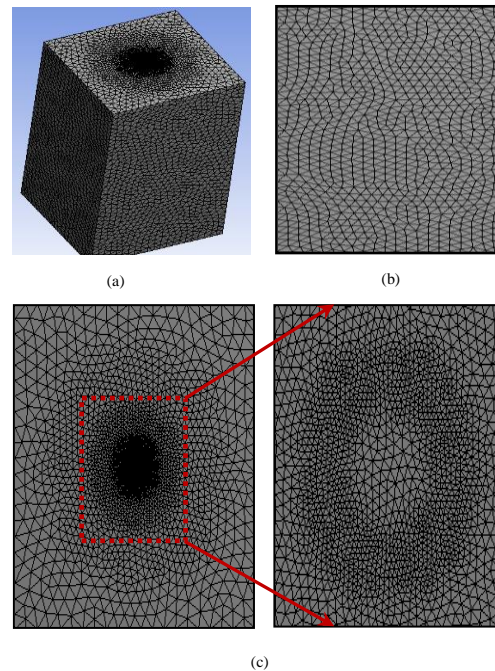
Fig. 4. Mesh structure for turbulent jet: (a) 3D geometry; (b) Side view and (c) Top view.

The mesh sensitivity test was based on the overall velocity field in order to select the optimum number of elements at which an effective solution can be obtained for the jet flow simulation. The mesh sensitivity was analyzed by changing the number of elements and evaluating the stability of velocity fields each time. Figure 6 shows the velocity fields obtained by varying the number of elements in the mesh. Large variations in the velocity fields were observed by using fewer elements while by
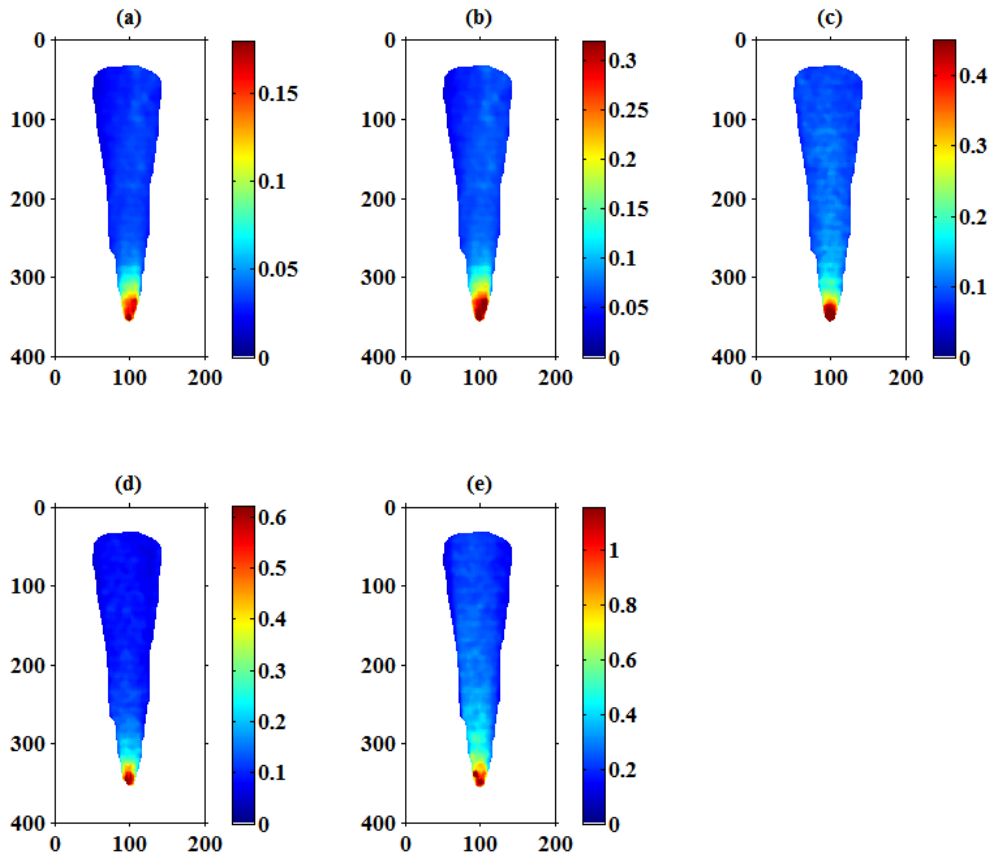
Fig. 5. Estimated image velocity field using FFT-based algorithm for different nozzle flow rates including: (a) $U_1 = 0.18$ m/s, (b) $U_2 = 0.32$ m/s, (c) $U_3 = 0.45$ m/s, (d) $U_4 = 0.62$ m/s and (e) $U_5 = 1.16$ m/s.

Table 2 Summary of boundary conditions used in the numerical simulation of the turbulent buoyant jet

No.	Description	Boundary condition
1	Nozzle velocity	0.18, 0.32, 0.45, 0.62 and 1.16 m/sec
2	Nozzle diameter	10 mm
3	Wall and output	Atmospheric pressure
4	Density of water	1000 kg/m3
5	The density of mixed water (5% salt)	1050 kg/m3

increasing the number of elements the velocity fields were observed to be stable.

To quantify the effect of mesh in velocity field simulation, the centerline velocity was used as bases for comparison. Figure 7 shows the normalized centerline velocity extracted from the velocity field (see Fig. 5) for different mesh densities. By increasing the mesh densities the velocity profiles become closer and insensitive to the mesh size, suggesting that the mesh resolution is adequate. Therefore, a mesh has 235,094 elements were used for the geometry meshing of turbulent jet flow. This mesh size was applied for all the cases of simulation runs.

2.6.4 Boundary Conditions

The boundary conditions used for turbulent buoyant jet simulation were taken to be same as the experimental conditions. A multi-phase fluid includes water and mixed-fluid were used to simulate the jet flow. The density of mixed fluid was changed by adding 5% of salt to the tap water, as done by Crone *et al.* (2008). Then, the jet flow was simulated by changing the nozzle velocity considering the same ranges of nozzle flow rates measured from experimental work. Table 2 summarized the boundary conditions that considered in numerical simulation of the turbulent buoyant jet.

2.6.4 Turbulent Buoyant Jet Model

Fluid flow is usually governed by the conservation laws which mainly include three fundamental variable quantities named as momentum, energy, and mass. Based on the second law of Newton, the rate of change of momentum equals the sum of the forces on a fluid particle. And based on the first law of thermodynamics, the rate of change of energy is equal to the sum of the rate of heat. Furthermore, the mass of a fluid is conserved (Versteeg & Malalasekera. 2007). The momentum equations control the fluid flow is the Navier–Stokes
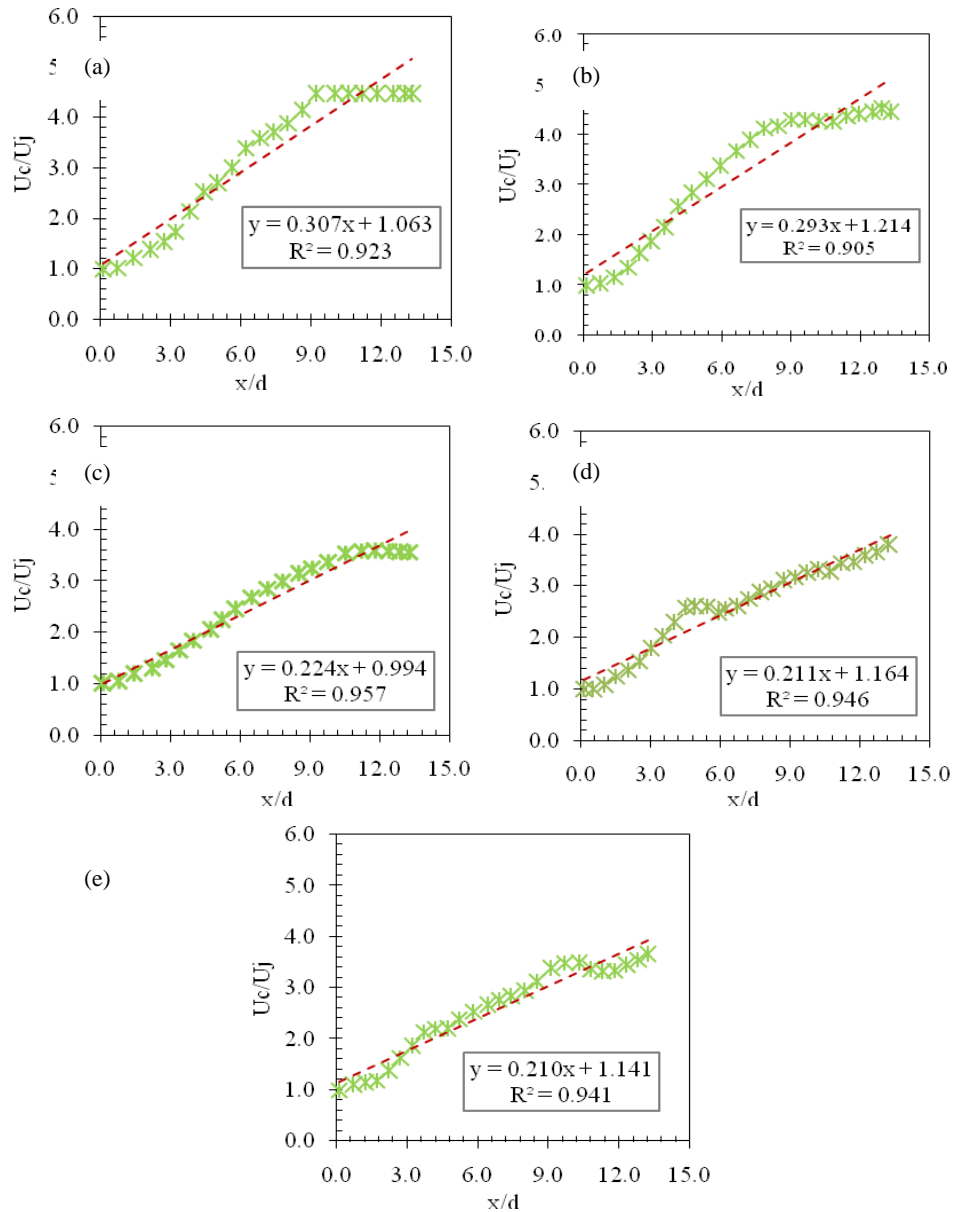
Fig. 6. Decay of centerline velocity for different nozzle velocity including (a) *U₁ = 0.18 m/s,* (b) *U₂ = 0.32 m/s,* (c) *U₃ = 0.45 m/s,* (d) *U₄ = 0.62 m/s* and (e) *U₅ = 1.16 m/s*.

equations. These equations are sets of non-linear differential equations that describe the flow of fluid whose stress depends linearly on flow velocity gradients and pressure.

CFD - Fluent solver includes several fluid models usually used for modeling the fluid flow. However, based on the previous investigation on common models used for simulating turbulent jet, it was found out that the standard k-epsilon model (Aziz, Raiford, and Khan. 2008). outperforms the others when tested with higher Reynolds number turbulent jet flow. The standard k- epsilon model produced the best result when used for simulating turbulent jet flow (Muppidi & Mahesh. 2005). The standard values for the k-epsilon model were used for jet flow simulation. Reynolds-Averaged Navier-stokes

can be formulated by the following equations:

$$\frac{\partial U_i}{\partial x_i} = 0 \tag{8}$$

$$\frac{\partial U_i}{\partial x_i} + U_j \frac{\partial U_i}{\partial x_i} = \frac{1}{\rho}\frac{\partial P}{\partial x_i}\frac{\partial}{\partial x_i}\left[\nu\frac{\partial U_i}{\partial x_i} - \overline{u_i u_j}\right] \tag{9}$$

where i,j are indices, x_i is the coordinate in which $i = 1,2,3$, U_i, U_j are time-averaged velocity components, t represents time (sec), ρ is the fluid density, P is the piezometric pressure, ν is the kinematic viscosity of the fluid, and $\overline{u_i u_j}$ the turbulent normal and shear stresses.
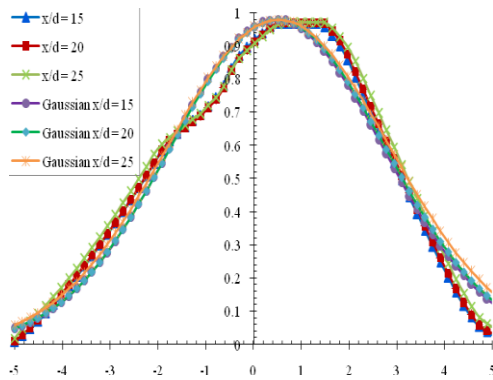
Fig. 7. Radial velocity at various axial distances for the case of nozzle velocity U1 = 1.16 m/sec.

The k-epsilon model is based on turbulent eddy viscosity to relate the normal-shear stresses to the time-averaged velocity gradients and turbulent kinetic energy by Eq. (10):

$$\overline{u_i u_j} = v_t \left(\frac{\partial U_i}{\partial x_j} + \frac{U_j}{\partial x_i} \right) - \frac{2}{3} k \, \delta_{ij} \tag{10}$$

where δ_{ij} is the Kronecker delta, and $k = 0.5\overline{u_i u_j}$ is the turbulent kinetic energy per unit mass, and v_t is the turbulent eddy viscosity and can be given by:

$$v_t = C_\mu \frac{k^2}{\varepsilon} \tag{11}$$

where C_μ is an empirical coefficient and *k-epsilon* is the dissipation rate of turbulent kinetic energy.

Then, $k - \varepsilon$ model, the k and ε can be formulated by the following two equations:

$$\frac{\partial k}{\partial t} + U_i \frac{\partial k}{\partial x_i} = \frac{\partial}{\partial x_i} \left(\frac{\partial v}{\sigma_k} \frac{\partial k}{\partial x_i} \right) + v_t \left(\frac{\partial U_i}{\partial x_j} + \frac{\partial U_j}{\partial x_i} \right) \frac{\partial U_i}{\partial x_j} - \varepsilon \tag{12}$$

$$\frac{\partial \varepsilon}{\partial t} + U_i \frac{\partial \varepsilon}{\partial x_i} = \frac{\partial}{\partial x_i} \left(\frac{v_t}{\sigma_\varepsilon} \frac{\partial \varepsilon}{\partial x_i} \right)$$
$$+ c_{1\varepsilon} \frac{\varepsilon}{k} v_t \left(\frac{\partial U_i}{\partial x_j} + \frac{\partial U_j}{\partial x_i} \right) \frac{\partial U_i}{\partial x_j} - c_{2\varepsilon} \frac{\varepsilon^2}{k} \tag{13}$$

where $c_\mu, c_{1\varepsilon}, c_{2\varepsilon} \, \& \, \sigma_k, \sigma_\varepsilon$ are empirical coefficients, and the standard values for these coefficients used in $k - \varepsilon$ the model are equal to 0.09, 1.44, 1.92, 1.0, and 1.3 respectively.

To solve these models two kinds of solvers are available when using CFD-FLUENT: the pressure-based and density-based coupled solvers. In this study, the pressure based solver is used for the numerical simulation of the jet flow. This because of the flexibility in the solution procedure and it requires less memory. The pressure-based solver is based on combining both velocity and pressure to solve the continuity and momentum equations in order to derive an equation for pressure correction. An algorithm called Semi-Implicit Method for Pressure-Linked Equations (SIMPLE) is used for solving these equations (Versteeg & Malalasekera. 2007).

Therefore, the velocity field obtained by numerical simulation will be compared with the outcomes of experimental works. First, a qualitative comparison of the overall velocity field that obtained as a result of simulation and experimental is conducted. Three parameters are also compared: jet growth rate, jet centerline velocity and self-similarity of radial velocity at various sections including *x/d* = 15, 20, and 25.

3. RESULTS AND DISCUSSION

3.1 Image Velocity Field

Figure 5 shows the estimated image velocity field using the FFT-based algorithm for different cases of nozzle flow rates. The color of velocity fields was adjusted from zero to the value of experimental nozzle velocity, so the velocity distribution can be compared to the predation of turbulent jet theory. The velocity has a similar distribution as the predicted with some variations. The maximum velocity was observed at the near-nozzle region, while the velocity seems to decay further from the nozzle. The velocity field has less noise, however, a short core jet with unsymmetrical distribution was observed in some cases of nozzle flow rates. This could be due to some problem associated with an input image sequence such as light variation.

Again, the estimated image velocity field was analyzed by extracting the centerline velocity and the profiles for radial velocity at the fully developed region of the jet. To validate the capability of the developed FFT-based algorithm in terms of estimating velocity field at the fully developed region, the self-similarity of the radial velocity is tested. The theory of turbulent jet flow suggests that self-similarity is associated with the radial velocity of different locations in the fully developed region and with a Gaussian distribution. The normalization of the radial velocity at any section in the fully developed region with its maximum usually results in Gaussian profiles.

3.2 Decay of Centerline Velocity

Figure 6 shows a decay of centerline velocity extracted from the image velocity field obtained by the FFT-based algorithm. This is for the five cases of nozzle velocity that were considered.

For all cases, a linear decay was observed for the centerline velocity in flow direction with small variations. The growth rate of centerline velocity was 3.3, 3.4, 4.5, 4.7 and 4.8 for the different cases of nozzle flow rate respectively. The FFT-based algorithm was able to distinguish between the different cases of nozzle flow rates. By increasing the nozzle flow rate, the jet growth rate was
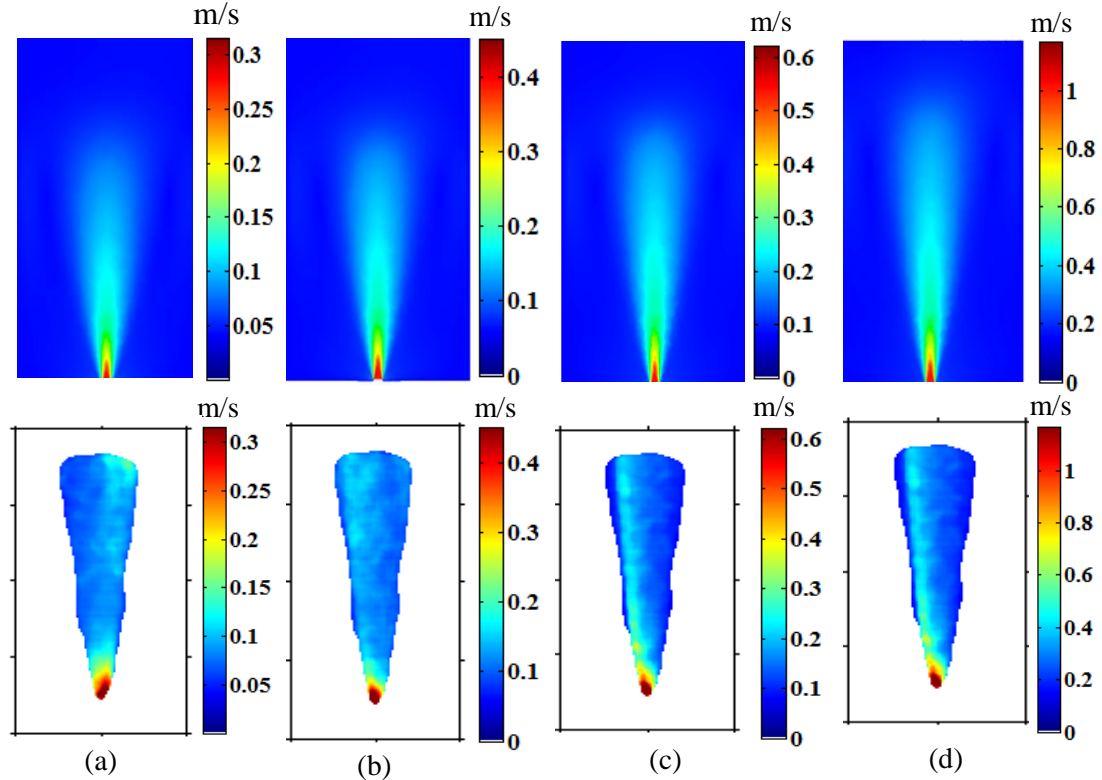
Fig. 8. Comparison of velocity field obtained by CFD simulation (top) and experiment (bottom) at different four cases of nozzle velocity including (a) $U_2 = 0.32$ m/s, **(b)** $U_3 = 0.45$ m/s, **(c)** $U_4 = 0.62$ m/s, **(d) and (e)** $U_5 = 1.16$ m/s.

increased. However, the magnitude of the growth rate was lower than the predicted. Lipari *et al.* (2011) found that the range of growth rate for free turbulent jet flow between 5.7 to 6.7 for higher nozzle flow rate. However, the growth rate ranges are acceptable since the maximum flow rate has a Reynolds number of 11,656 while in most of the available literature deal with higher flow rates.

3.3 Radial Velocity

Figure 7 shows a relation between normalized radial velocity at three different axial distance selected at the fully developed region of the jet flow including, x/d = 15, 20 and 25. The normalization of the velocity distribution at a different axial distance by the centerline velocity should provide a self-similarity property in which a Gaussian distribution is predicted. All the radial velocities extracted from the velocity field obtained by the FFT-based algorithm are in a good agreement with the predicted Gaussian profiles. However, the velocity distributions have a similar trend with small differences, as compared to the Gaussian profiles. Moreover, the peak positions of theoretical radial velocity seen at the center, while for the estimated profiles deviated either left or right. This is acceptable since there are some uncertainties in the estimation of velocity field which associated with the input image sequences.

3.4 Comparison between Experimental and Simulation Outcomes

A comparison between the experimental and CFD simulation outcomes is presented in this section. All image velocity fields which were estimated using the FFT-based algorithm were converted to the center plane. Then, a comparison can be done between the experimental and simulation outcomes. The centerline velocity, growth rates, and the radial velocity which estimated by the FFT-based algorithm (experiment) and from CFD simulation were compared.

3.4.1 Qualitative Comparison of Velocity Fields

Figure 8 shows a comparison of the velocity fields obtained from experimental works with the CFD simulation. The color of the velocity field was adjusted from zero up to the experimental value. In the near-nozzle jet region, there is a good agreement between experimental and simulation results, since the region has a velocity magnitude closer to the actual nozzle velocity. However, a short core length was observed for experimental results as compared to the long cores of CFD simulation. Furthermore, symmetrical velocity distributions were observed in the near-nozzle region for the numerical simulation, while for the experimental results, the velocity distributions were not totally symmetric.
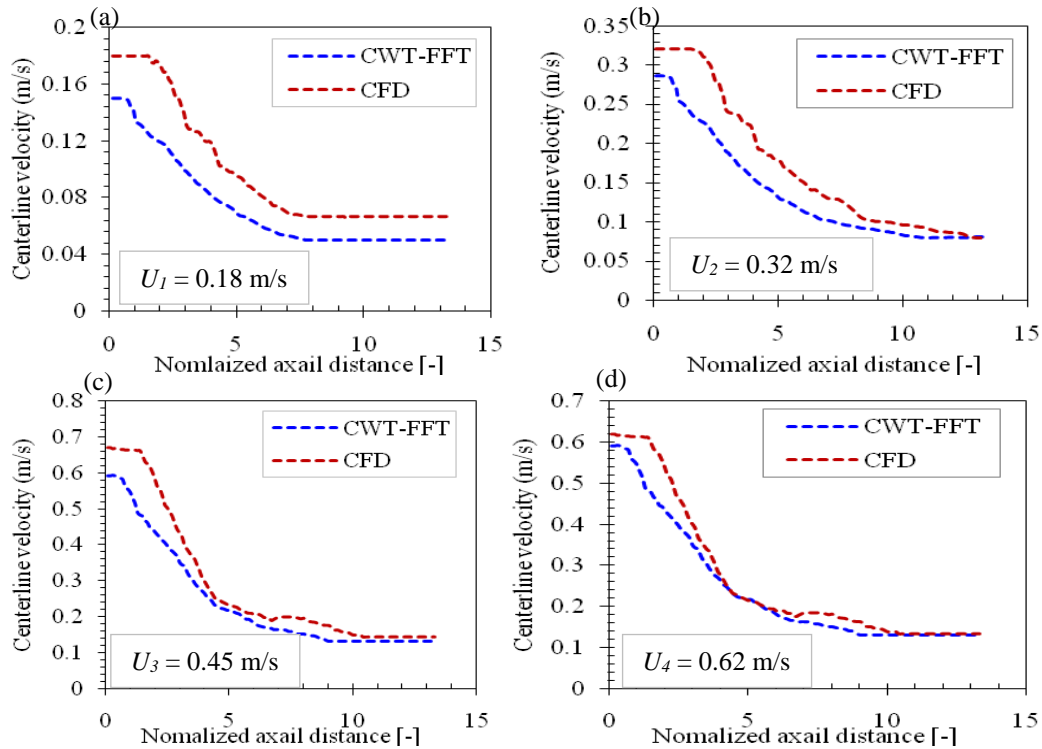
Fig. 9. Comparison of axial centerline velocity between experiment and numerical simulation for the five different cases of nozzle flow rates including (a) U1 = 0.18 m/s, (b) U2 = 0.32 m/s, (c) U3 = 0.45 m/s, (d) U4 = 0.62 m/.

Fast velocity decay was observed in flow direction for the experimental velocity field, while the velocity field was gradually decayed in case of simulation results and it was smooth. The propagation of the jet flow was mainly based on the nozzle velocity in which by increasing the nozzle velocity, the flow propagation increases. Moreover, the results obtained from simulation confirmed the self-similarity property of turbulent jet flow as the predicted. Meanwhile, for the experimental velocity field, the velocity distribution was not symmetrical as observed for the left and right side of the jet.

3.4.2 Centerline Velocity

Figure 9 shows a comparison between the axial centerline velocities extracted from the velocity fields obtained by the FFT-based algorithm as compared to the centerline velocity obtained by CFD simulation. For all the cases, the centerline velocity from the experimental work has the same trend as compared to the velocity trend from CFD simulation. The estimated centerline velocity from the experiment was also less than that obtained from CFD. However, large differences were observed in the pure jet region.

This difference, however, was seen to reduce with increasing the axial distance of the jet after which the centerline velocity decay rate became constant. The differences represented errors of 14.3%, 9.4%, 9.7%, 8.3% and 12.7% for the nozzle flow rate cases of Q1, Q2, Q3, Q4, and Q5 respectively.

Therefore, the velocity field which was obtained by the FFT-based method was less than the outcomes of numerical simulation. This is acceptable since the estimation was based on the jet surface which slower velocities were expected as compared to the jet core region.

Table 3 shows a comparison of the jet growth rates obtained from experimental work as compared to the numerical simulation. A good agreement small difference between the growth rates of the FFT-based algorithm and simulation were observed.

Table 3 Comparison of centerline velocity decay rate between experiment and CFD simulation

No.	Flow rate	Growth rate		
		CFD	Experiment	Difference (%)
1	Q1	3.6	3.3	8.3%
2	Q2	3.8	3.4	10.5%
3	Q3	4.5	4.5	0.0%
4	Q4	4.9	4.7	4.1%
5	Q5	5.04	4.8	4.8%

3.4.3 Radial Velocity

The radial velocity profile at the nozzle obtained from the CFD simulation was validated with that obtained from the experimental study. The velocity profiles were taken at various flow rates and axial

(a)

(b)

(c)

(d)

(e)
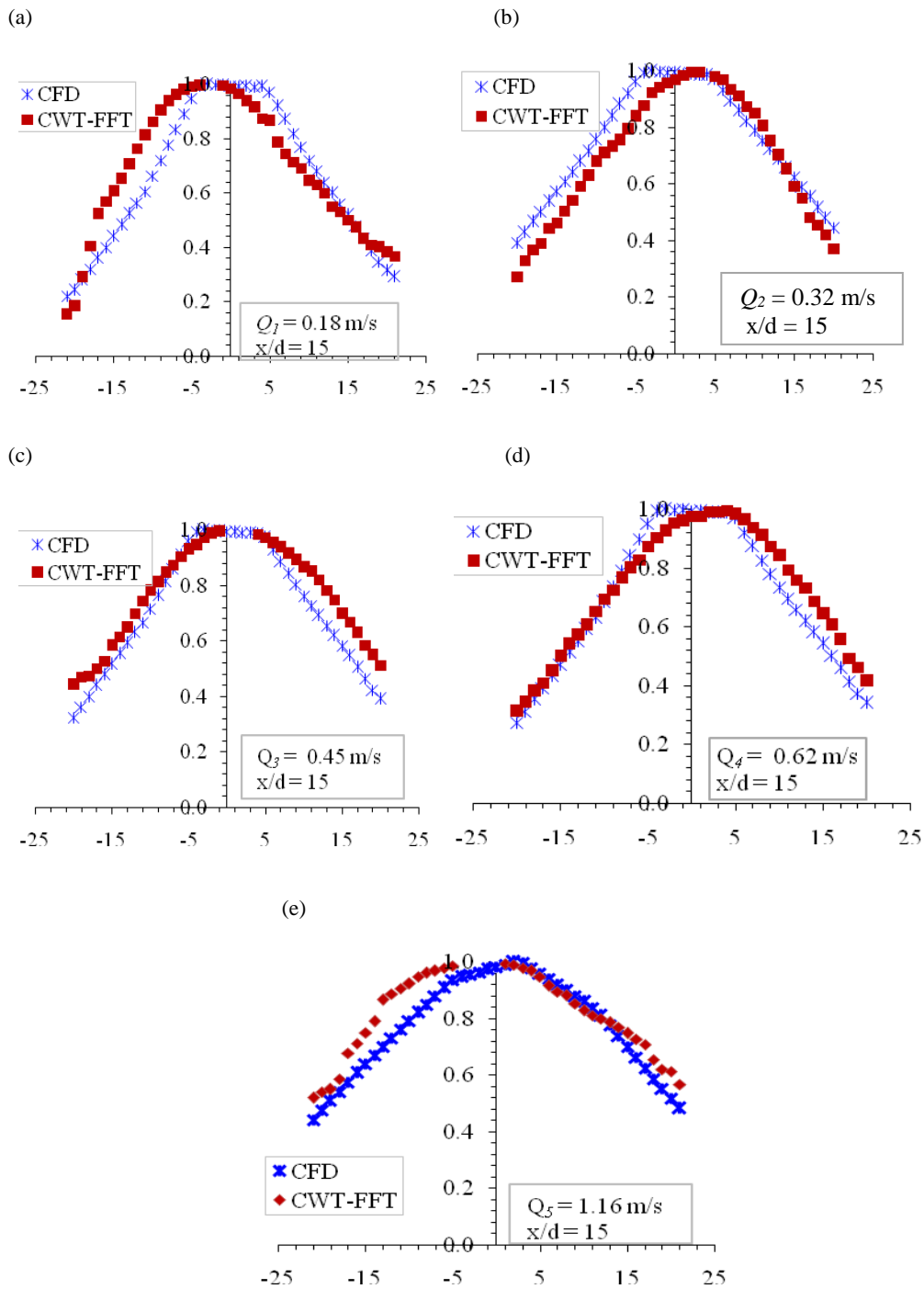
Fig. 10. Comparison of radial velocity from CWT-FFT and CFD at x/d = 10 for various flow rates: (a) U₂ = 0.32 m/s, (b) U₃ = 0.45 m/s, (c) U₄ = 0.62 m/s, (d) and (e) U₅ = 1.16 m/s.

distances. Figure 10 presents the comparison of the profiles from the two methods taken at different flow rates and *x/d =15*. There is a good match between the two profiles with a mean percentage error of 13.0%, 9.8%, 8.0%, 8.2% and 10.3% at 0.18 m/s, 0.32 m/s, 0.45, 0.62, and 1.16 m/s respectively.

4. CONCLUSION

Experimental and numerical simulation analyses

were conducted to investigate the characteristic of the turbulent buoyant jet at various nozzle flow rates with Reynolds number at jet exist ranged from 1847 to 11,656. An image velocity fields were estimated using the FFT-based algorithm. The FFT-based algorithm was estimated the nozzle flow rates with an error of 18.2% when compared to the measured experimental flow rates. The FFT method estimation results showed good results at the near-nozzle region as compared to the outcome of CFD simulation in this region. Despite good agreement

were observed between FFT estimation and CFD simulation, in term of centerline velocity and radial velocity where similar trends. However, poor results were obtained at a fully developed region far from the nozzle. The large difference is due to the large error associated with FFT based algorithm as well as the uncertainty of experimental works which generated a noisy jet video. To overcome this problem a new algorithm based on a defined wavelet coefficients will be developed. This is in order to remove noise from turbulent signals prior cross correlation step, which will help to improve the accuracy of flow estimation.

ACKNOWLEDGMENTS

REFERENCES

Abdel-Rahman, A. (2010). A review of effects of initial and boundary conditions on turbulent jets. *SEAS Transactions on Fluid Mechanics* 4, 257-275.

Adrian, R. J. (1991). Particle-imaging techniques for experimental fluid mechanics. *Annual review of fluid mechanics* 23, 261-304.

Akselvoll, K. and P. Moin (1996). Large-eddy simulation of turbulent confined co-annular jets. *Journal of Fluid Mechanics* 315, 387-411.

Aziz, T., J. Raiford and A. Khan. (2008). Numerical simulation of turbulent jets. *Engineering applications of computational fluid mechanics* 2, 234-243.

Bailey, S., M. Hultmark, J. Monty, P. H. Alfredsson, M. Chong, R. Duncan, et al. (2013). Obtaining accurate mean velocity measurements in high Reynolds number turbulent boundary layers using Pitot tubes. *Journal of Fluid Mechanics* 715, 642.

Bradshaw, P. (1966). The effect of initial conditions on the development of a free shear layer. *Journal of Fluid Mechanics* 26, 225-236.

Chue, S. (19750). Pressure probes for fluid measurement. *Progress in aerospace sciences* 16, 147-223.

Crone, T. J., R. E. McDuff and W. S. Wilcock (2008). Optical plume velocimetry: A new flow measurement technique for use in seafloor hydrothermal systems. Experiments in Fluids, vol. 45, pp. 899-915.

Dziomba, B. and H. Fiedler (1985). Effect of initial conditions on two-dimensional free shear layers. *Journal of Fluid Mechanics* 152, 419-442.

Gilbert, R. and Johnson, D. (2003). Evaluation of FFT-based cross-correlation algorithms for PIV in a periodic grooved channel. *Experiments in Fluids* 34, 473-483.

Kannan B., S. Karthikeyan and S. Sundararaj (2017). Comparison of Turbulence Models in Simulating Axisymmetric Jet Flow. *Innovative Design and Development Practices in Aerospace and Automotive Engineering, Springer* 401-407.

Kannan, B. T., S. Karthikeyan and S. Sundararaj (2017). Comparison of Turbulence Models in Simulating Axisymmetric Jet Flow. *In Innovative Design and Development Practices in Aerospace and Automotive Engineering, Singapore: Springer Singapore* 401-407.

Lehr, B., A. Aliseda, P. Bommer, P. Espina, O. Flores, J. Lasheras, et al. (2010). Deepwater horizon release estimate of rate by PIV. Report to the US Dept of interior.

Lipari, G. and P. K. Stansby. (2011). Review of experimental data on incompressible turbulent round jets. *Flow, turbulence and combustion* 87, 79-114.

McNutt, M. K., R. Camilli, G. D. Guthrie, P. A. Hsieh, V. F. Labson, W. J. Lehr, et al. (2011). Assessment of flow rate estimates for the Deepwater Horizon/Macondo well oil spill: US Department of the Interior.

McNutt, M. K., R. Camilli, T. J. Crone, G. D. Guthrie, P. A. Hsieh, T. B. Ryerson, et al. (2012). Review of flow rate estimates of the Deepwater Horizon oil spill. *Proceedings of the National Academy of Sciences* 109, 20260-20267.

Mi, J. and G. Nathan (2010). Statistical properties of turbulent free jets issuing from nine differently-shaped nozzles. *Flow, turbulence and combustion* 84, 583-606.

Mi, J., D. Nobes and G. Nathan (2001). Influence of jet exit conditions on the passive scalar field of an axisymmetric free jet. *Journal of Fluid Mechanics* 432, 91-125.

Mi, J., G. Nathan and R. Luxton (2000). Centreline mixing characteristics of jets from nine differently shaped nozzles. *Experiments in Fluids* 28, 93-94.

Mi, J., P. Kalt, G. Nathan and C. Wong (2007). PIV measurements of a turbulent jet issuing from round sharp-edged plate. *Experiments in Fluids* 42, 625-637.

Miller, R. W. (1983). *Flow measurement engineering handbook.*

Muppidi, S. and K. Mahesh. (2005). Direct numerical simulation of turbulent jets in crossflow. *In 43rd AIAA Aerospace Sciences Meeting and Exhibit* 1115.

Otsu, N. (1975). A threshold selection method from gray-level histograms. *Automatica* 11, 23-27.

Pust, O. (2000). PIV: Direct cross-correlation compared with fft-based cross-correlation.

Proceedings of the 10th International Symposium on Applications of Laser Techniques to Fluid Mechanics, Lisbon, Portugal 114.

Quinn, W. (2006). Upstream nozzle shaping effects on near field flow in round turbulent free jets. *European Journal of Mechanics-B/Fluids* 25, 279-301.

Quinn, W. (2007). Experimental study of the near field and transition region of a free jet issuing from a sharp-edged elliptic orifice plate. *European journal of Mechanics-B/Fluids* 26, 583-614.

Shih, T.-H., W. W. Liou, A. Shabbir, Z. Yang and J. Zhu (1995). A new k-ϵ eddy viscosity model for high Reynolds number turbulent flows. *Computers & Fluids* 24, 227-238.

Sorbe, J. (2014). An experimental study in the near field of a turbulent round free jet. MSc thesis, University of GAVLE.

Spalart, P., W. Jou, M. Strelets and S. Allmaras (1997). Comments on the feasibility of LES for wings, and on a hybrid RANS/LES approach. *Advances in DNS/LES* 1, 4-8.

Stainback P. and K. Nagabushana. (1993). Review of hot-wire anemometry techniques and the range of their applicability for various flows. 1, 4.

Tian, X. and P. J. Roberts (2003). A 3D LIF system for turbulent buoyant jet flow. *Experiments in Fluids* 35, 636-647.

Uddin, M. and A. Pollard (2007). Self-similarity of coflowing jets: the virtual origin. *Physics of Fluids* 19, 068103.

Versteeg, H. K. and W. Malalasekera. (2007). An introduction to computational fluid dynamics: the finite volume method. *Pearson Education.*

Wang, Z., P. He, Y. Lv, J. Zhou, J. Fan and K. Cen (2010). Direct numerical simulation of a subsonic round turbulent jet. *Flow, turbulence and combustion* 84, 669-686.

Westerweel, J. (1994). Efficient detection of spurious vectors in particle image velocimetry data. *Experiments in Fluids* 16, 236-247.

Wygnanski, I. and H. Fiedler (1969). Some measurements in the self-preserving jet. *Journal of Fluid Mechanics* 38, 577-612.

Yakhot, V., S. Orszag, S. Thangam, T. Gatski and C. Speziale (1992). Development of turbulence models for shear flows by a double expansion technique. *Physics of Fluids A: Fluid Dynamics* 4, 1510-1520.